

NUMERICAL SIMULATION OF THERMALLY RADIATIVE AND EMHD INFLUENCED VISCOPLASTIC FLUID FLOW: A SECOND LAW INVESTIGATION

K. DEEPA

Department of Mathematics, Shiv Nadar University Chennai, Kalavakkam 603110 Tamilnadu, India
E-mail: deepakkrish1@gmail.com

Received May 31, 2023

Abstract. This work rigorously presents the findings of entropy generation in Casson fluid flow on a Riga plate, exposed in a radiative environment. The conceptual basis for the investigation of fluid flow is the system of governing boundary layer equations. By means of implicit finite difference procedure the solutions of boundary layer equations are acquired. Primary goal of this study manifests the optimization of entropy generation in Casson fluid flow associated with EMHD (Electro Magneto Hydro Dynamics) Lorentz force and thermal radiation. Additionally, the contours of entropy generation and Bejan number are demonstrated. Validation of present results with previously obtained results from literature is accomplished conscientiously.

Key words: entropy, Riga plate, Casson fluid.

DOI: <https://doi.org/10.59277/RomJPhys.2023.68.117>

1. INTRODUCTION

The mechanism of irreversibility due to entropy generation is encountered during the heat energy transport between a surface and fluid flow. The conception of entropy owes to the second law of thermodynamics. The possession of disordered movement of atoms during the dissipation of energy in the system leads to a non-conserved phenomenon and depletion of energy. Thus, the investigation of change in entropy ascertains the system's efficiency. The molecular heat conduction and viscous dissipation most prominently influence the generation of entropy. Following this, radiative heat transport also paves the way to the major challenging entropy environment. Selamet and Arpaci [1] discussed the radiation-influenced entropy distribution.

Bejan [2] reviewed the results on entropy minimization. The effects of slip on momentum and production of entropy with respect to fluid flow over a plate associated with the convective boundary were explored by Butt *et al.* [3]. Ellahi *et al.* [4] performed a similar work on a moving plate defying a convective boundary and it was reported that upliftment in slip parameter diminished the entropy. On the other hand, the investigation contingent on slip boundary of a stretching sheet for non-Newtonian fluid flow elucidated an increase in entropy generation [5]. Erbay *et al.* [6, 7] analysed the entropy generation for flow through parallel plated.

The efficacy of suction and blowing to curb the influence of irreversibility in the system was reported for a flow past a permeable plate by Reveillere and Baytas [8]. Esfahani and Jafarian [9] scrutinized the distribution of entropy for the Blasius series solution, Integral solution, and similarity solution of boundary layer equations that govern the flow on a flat plate. Matin [10] estimated the irreversibility characteristics of boundary layer flow on a plate saturated in a porous membrane. Ferhi and Djebali [11] studied the second law analysis of microflows.

The Newtonian fluid's behaviour can be seen in the friction law, which relates shear stress with shear rate. A non-Newtonian fluid is one that deviates from this linear constitutive equation. Biological fluids, paints, drilling fluids, paint thinners, thermoplastics, polymer solutions, and paints are some classic non-Newtonian fluids [12]. Amidst the various non-Newtonian fluids, Casson fluid is the most widely used viscoplastic fluid which explicates a negligible viscosity subject to higher shear rate. The nonlinear relationship between shear stress and the deformation rate was constructed by Casson during the analysis of the pigment oil suspension in printing ink [13].

Many literatures focused on Casson fluid because of its wide variety of applications. The flow of blood in an artery can also be modelled as a Casson fluid flow problem. Through the perturbation method, Chaturani and Samy [14] investigated the non-Newtonian model of blood flow in stenosed arteries. Srivatsava and Saxena [15] designed a two-layered Casson fluid model that can be applied in the clinical findings of cardiovascular dysfunction. Dash *et al.* [16] presented the flow behaviour of Casson fluid in a tube subject to homogeneous perforated material. A mathematical model of thermal energy and entropy analysis for the buoyancy driven Casson fluid flow through a deformable perforated layer was proposed by Gopi Krishna *et al.* [17]. Mansour *et al.* [18] attempted the second law analysis of Casson fluid flow past a stretching sheet in an unsteady physical situation.

When the flow field is subjected to the combined impact of electric and magnetic forces, electromagnetic forces are produced. The proposed Electro Magneto Hydro Dynamics (EMHD) analogy is related to the actuator known as the Riga plate, which is configured by the alternative configuration of electrodes and magnets. Gailitis and Lielausis named and constructed this actuator to stabilize the adverse effect of boundary layer separation. Posdziech and Grundmann [19] reported that EMHD could shrink surface skin friction. The favourable phenomenon of flow speed in relation to Lorentz force was investigated by Magyari and Pantokratoras [20] and the solutions of the flow model were obtained using a finite difference scheme. Along with MHD or EMHD Lorentz force, Pantokratoras [21] determined the precise solution of the Blasius-Sakiadis flow. Loganathan and Deepa [22, 23] computed the numerical solution and exact solution for the convective Casson fluid flow under an EMHD environment. Rafique *et al.* [24] and Rooman *et al.* [25] constructed micropolar nanofluid and Williamson nanofluid model on EMHD actuator.

Early on, the magnetic field's influence was used in processing units for industrial processes like melting and solidification. Due to recent technological developments, the interaction of electric and magnetic fields (EMHD) is much more effective in controlling the melting and solidification processes. The induced Lorentz force unveils the massive impact on solidification while considering the irreversibility effects. Shah *et al.* [26] accentuated that the Lorentz force can be employed to equilibrate the irreversible process, and which stimulates the solidification rate of nanoparticles-enhanced phase change material where the Lorentz force has been generated by subsuming magnetic field alone in the system.

Nevertheless, the present theoretical exposition on EMHD would break the ground by optimizing the entropy with the aid of streamwise Lorentz force in a viscoplastic fluid medium. The rapid solidification can also be achieved by means of controlling entropy production. Wang *et al.* [27] proposed an interface model for solidification process within which the maximization of entropy is adopted. As a matter of fact, the combination of chemical kinetics and irreversible effects leads to the major application of crystal growth [28]. Thus, the current research work can be effectively implemented together with chemical reactions in the field of crystallization.

Most often, the complexity arises due to entropy in a radiative environment and the computation of irreversibility ratio have received less attention among many researchers. In a relatively simple way, the primary goal of this proposed elucidation involves the incompressible Casson fluid flow on a moving Riga plate to optimize the entropy production. In specific, the visualization of entropy and Bejan number through the contour slices and the two-dimensional plots of time dependent variations of the quantities are the indispensable idiosyncrasies of this work.

2. MATHEMATICAL ANALYSIS

The thermally radiative Casson fluid flow over a vertical Riga-plate under free convection is schematically represented with a coordinate system in Fig. 1a and b. At the outset, the plate is inert, the velocity of the flow is zero and the thermal condition is at free stream level. In the still fluid, the plate starts to ascend in an upward direction at a constant speed u_0 for $t' > 0$ against the gravitational force. Compared to the conditions at the wall (T'_w), the surrounding fluid's temperature (T'_∞) is lower. The temperature falls to asymptotic levels and the velocity decays to zero in the case where the flow is far from the plate. It is presumed that the fluid flows along x direction and the transverse direction is y with the corresponding velocities u and v respectively. Fluid properties are constant except for the buoyancy force. Direction is insignificant in radiative flux and scattering is neglected. The stress strain behaviour of Casson fluid is recounted as follows [29, 30].

$$\tau_{ij} = \begin{cases} 2 \left(\mu_b + \frac{P_y}{\sqrt{2\pi^*}} \right) e_{ij}, \pi^* > \pi_c^* \\ 2 \left(\mu_b + \frac{P_y}{\sqrt{2\pi_c^*}} \right) e_{ij}, \pi^* \leq \pi_c^* \end{cases}$$

Here, $\pi^* = e_{ij} e_{ij}$, π_c^* is its critical value and e_{ij} is the $(i, j)^{\text{th}}$ component of the shear rate, μ_b, P_y are the plastic dynamic viscosity and yield stress of the fluid, respectively.

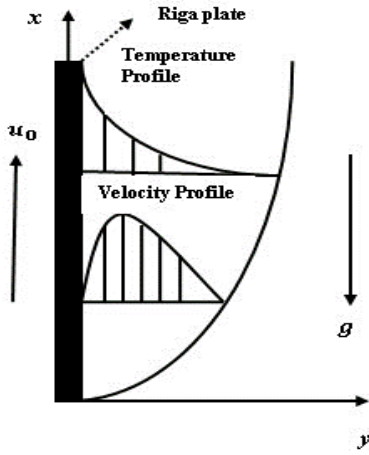


Fig. 1a – Flow description of the model.

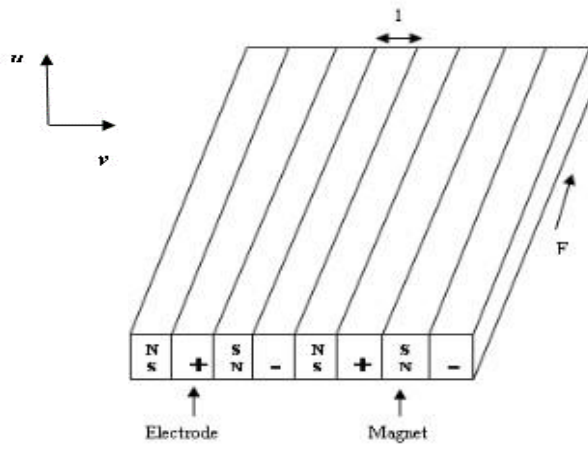


Fig. 1b – Construction of Riga plate.

The flow model comprises of the above assumptions is fabricated mathematically as a coupled non-linear system of partial differential equations.

$$\frac{\partial u}{\partial x} + \frac{\partial v}{\partial y} = 0 \quad (1)$$

$$\frac{\partial u}{\partial t'} + u \frac{\partial u}{\partial x} + v \frac{\partial u}{\partial y} = \nu \left(1 + \frac{1}{\beta} \right) \frac{\partial^2 u}{\partial y^2} + g \beta' (T' - T'_\infty) + \frac{\pi J_0 M_0 \exp(-\pi y/l)}{8\rho} \quad (2)$$

$$\frac{\partial T'}{\partial t'} + u \frac{\partial T'}{\partial x} + v \frac{\partial T'}{\partial y} = \alpha \frac{\partial^2 T'}{\partial y^2} - \frac{1}{\rho C_p} \frac{\partial q_r}{\partial y} + \frac{\mu}{\rho C_p} \left(\frac{\partial u}{\partial y} \right)^2. \quad (3)$$

Initial and boundary conditions of the flow problem are

$$\begin{aligned}
 t' \leq 0, \quad u = 0, \quad v = 0, \quad T' = T'_\infty \quad \text{for all } x \text{ and } y, \\
 t' > 0, \quad u = u_0, \quad v = 0, \quad T' = T'_w \quad \text{for } y = 0, \\
 u = 0, \quad v = 0, \quad T' = T'_\infty \quad \text{for } x = 0, \\
 u \rightarrow 0, \quad T' \rightarrow T'_\infty \quad \text{as } y \rightarrow \infty.
 \end{aligned} \tag{4}$$

Here the Casson parameter is described as $\beta = \frac{\mu_b \sqrt{2\pi_c^*}}{P_y}$. Variation in

radiative flux $\frac{\partial q_r}{\partial y} = -\frac{16\sigma' T_\infty'^3}{3a^*} \frac{\partial^2 T'}{\partial y^2}$ is pointing towards the direction normal to the

plate and it can be approximated using Rosseland approximation $q_r = -\frac{4\sigma'}{3a^*} \frac{\partial T'^4}{\partial y}$ [31, 32]. The parameters that are involved in non dimensionalizing the governing equations (1), (2), (3) and (4) are mentioned below.

$$\begin{aligned}
 X = \frac{xu_0}{\nu}, \quad Y = \frac{yu_0}{\nu}, \quad U = \frac{u}{u_0}, \quad V = \frac{v}{u_0}, \quad t = \frac{t' u_0^2}{\nu}, \quad T = \frac{T' - T'_\infty}{T'_w - T'_\infty}, \\
 Gr = \frac{\nu g \beta' (T'_w - T'_\infty)}{u_0^3}, \quad Pr = \frac{\nu}{\alpha}, \quad R^* = \frac{\kappa a^*}{4\sigma' T_\infty'^3}, \quad Br' = \frac{\mu u_0^2}{\kappa (T'_w - T'_\infty)}
 \end{aligned} \tag{5}$$

The normalization yields the equations (1), (2), (3) and (4) in non-dimensional form

$$\frac{\partial U}{\partial X} + \frac{\partial V}{\partial Y} = 0, \tag{6}$$

$$\frac{\partial U}{\partial t} + U \frac{\partial U}{\partial X} + V \frac{\partial U}{\partial Y} = \left(1 + \frac{1}{\beta}\right) \frac{\partial^2 U}{\partial Y^2} + GrT + Ha^* e^{-sY}, \tag{7}$$

$$\frac{\partial T}{\partial t} + U \frac{\partial T}{\partial X} + V \frac{\partial T}{\partial Y} = \frac{1}{Pr} \left(\left(1 + \frac{4}{3R^*}\right) \frac{\partial^2 T}{\partial Y^2} + Br' \left(\frac{\partial U}{\partial Y}\right)^2 \right). \tag{8}$$

Initial and boundary conditions are

$$\begin{aligned} t \leq 0, U = 0, V = 0, T = 0 \text{ for all } X \geq 0 \text{ and } Y \geq 0, \\ t > 0, U = 1, V = 0, T = 1 \text{ for } Y = 0, \\ U = 0, V = 0, T = 0 \text{ for } X = 0, \\ U \rightarrow 0, T \rightarrow 0 \text{ as } Y \rightarrow \infty. \end{aligned} \quad (9)$$

2.1. COMPUTATION OF ENTROPY PRODUCTION

In a reversible process, there is no indication of entropy generation whereas for an irreversible process combined with radiative flux, the local entropy generation [1] is computed to be

$$S_{gen} = \frac{1}{T_w'} \left\{ \frac{1}{T_\infty'} \left(\kappa \left(\frac{\partial T'}{\partial y} \right) + \frac{4\sigma'}{3a^*} \left(\frac{\partial T'^4}{\partial y} \right) \right) \left(\frac{\partial T'}{\partial y} \right) + \mu \left(1 + \frac{1}{\beta} \right) \left(\frac{\partial u}{\partial y} \right)^2 \right\} \quad (10)$$

Approximating the fourth power of temperature, the equation (10) yields

$$S_{gen} = \frac{1}{T_w'} \left\{ \frac{1}{T_\infty'} \left(\kappa \left(\frac{\partial T'}{\partial y} \right) + \frac{16\sigma' T_\infty'^3}{3a^*} \left(\frac{\partial T'}{\partial y} \right) \right) \left(\frac{\partial T'}{\partial y} \right) + \mu \left(1 + \frac{1}{\beta} \right) \left(\frac{\partial u}{\partial y} \right)^2 \right\} \quad (11)$$

Applying the non-dimensional parameters stated in (5) on the above equation (11)

$$N_S^* = \left(1 + \frac{4}{3R^*} \right) \left(\frac{\partial T}{\partial Y} \right)^2 + Br^* \left(1 + \frac{1}{\beta} \right) \left(\frac{\partial U}{\partial Y} \right)^2 \quad (12)$$

$N_S^* = \frac{S_{gen}}{S_G}$ is the non-dimensional entropy generation, $S_G = \frac{\kappa u_0^2 (T_w' - T_\infty')^2}{\gamma^2 T_\infty'^2}$ is the

characteristic entropy generation rate and $Br^* = \frac{\mu u_0^2 T_\infty'}{\kappa (T_w' - T_\infty')^2}$ is the modified

Brinkmann number. The two terms appear in equation (12) unveils the entropy production by means of heat transfer (N_H^*) and fluid friction (N_F^*) respectively. To comprehend the process of entropy production, the irreversibility emerge from the thermal transport and flow field are examined through the irreversibility ratio

termed as Bejan number (Be) which delineates the relationship between thermal entropy production and the aggregate of entropy generation.

$$Be = \frac{N_H^*}{N_S^*} = \frac{1}{1 + \frac{N_F^*}{N_H^*}}. \quad (13)$$

The value of Bejan number analyses the intensity of entropy generated because of heat transfer and fluid friction. $Be < 0.5$, when there is a substantial entropy production due to heat transfer. For the case of higher influence from fluid friction, the Bejan number hits the value in $Be > 0.5$, wherein $Be = 0.5$, while the two quantities are proportionate. Further, it is evident that the Bejan number varies between 0 and 1.

3. NUMERICAL SOLUTION

The new set of dimensionless governing partial differential equations (6), (7), (8), (9), (12) and (13) embrace the Crank-Nicholson implicit finite difference method [33] to acquire the solutions. The rectangular solution domain is pondered for $X_{\max} = 1.0$, $Y_{\max} = 14.0$. Y_{\max} indicates the value of Y when the fluid particles are at distant from the plate. Mesh generation is performed with uniform grid spacing for $\Delta X = 0.02$, $\Delta Y = 0.25$ and Δt time steps. Mesh sizes are chosen with the aid of grid independence of solution. Thomas algorithm is adopted to solve the tridiagonal system gleaned from finite difference equations.

At $(m + 1)^{th}$ time level, the momentum, thermal energy and solutal concentration values are procured for each grid point. The steady state solutions are attained when consecutively two iterations possess a difference of 10^{-5} . While ΔX , ΔY and $\Delta t \rightarrow 0$ the local truncation error vanishes. This confirms that the scheme is compatible. Further, the convergence is guaranteed by the stability and compatibility. The numerical results of skin friction, Nusselt number, Bejan number and entropy generation are also derived. The expressions of local and average skin friction, Nusselt number are listed below.

$$\begin{aligned} \tau_x &= -\left(1 + \frac{1}{\beta}\right) \left(\frac{\partial U}{\partial Y}\right)_{Y=0}, \quad \bar{\tau} = -\int_0^1 \left(1 + \frac{1}{\beta}\right) \left(\frac{\partial U}{\partial Y}\right)_{Y=0} dX, \\ Nu_x &= -X \left(\frac{\partial T}{\partial Y}\right)_{Y=0}, \quad \bar{Nu} = -\int_0^1 \left(\frac{\partial T}{\partial Y}\right)_{Y=0} dX, \end{aligned} \quad (14)$$

4. RESULTS AND DISCUSSION

The results of Pantokratoras and Magyari [34] and Gebhart and Pera [35] are correlated with the observed values of this investigation. This comprehensive comparison guarantees the physical postulates elucidated in the proposed and existing solutions, and Fig. 2 illustrates it. Correlation between the temperature is established through the results of Gebhart and Pera [35]. The velocity distribution displays a perfect fit for Pantokratoras and Magyari.

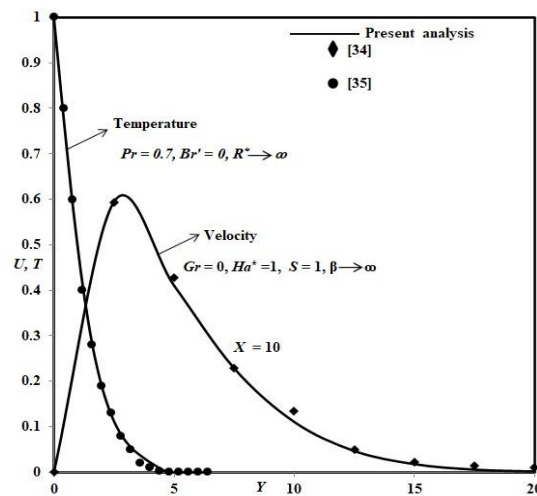


Fig. 2 – Comparison of flow field with [34, 35].

Figure 3 displays the velocity variations for different values of modified Hartmann number and radiation parameter over steady state time. Ha^* values that are positive indicate an aiding flow. Thus, the assisting flow exhibits an increase in flow rate as the Lorentz's force is acting in the direction of the fluid flow. Nevertheless, emission of radiation slows down the assisting flow. Also, the steady state time enters a quicker phase as the velocity shoots up with respect to the impact of modified Hartmann number and radiation parameter.

Thermal energy associated with the changes in different parameters is depicted in Fig. 4. The transit of electrons in magnets and electrodes is governed by radiation. This indicates that when radiation parameter R^* increases, the temperature decreases. The modified Hartmann number Ha^* relies upon the magnetization and current density. Elevated values of Ha^* indicate the increase in magnetization. Therefore, the strength of the magnetic field diminishes the temperature. On the other hand, Br' rises the temperature for larger values. However, the solution reaches the steady state rapidly for improved values of Br' , R^* and at a slower phase for Ha^* .

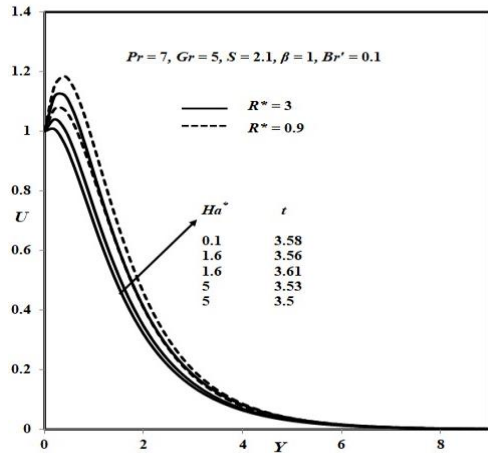


Fig. 3 – Velocity distribution.

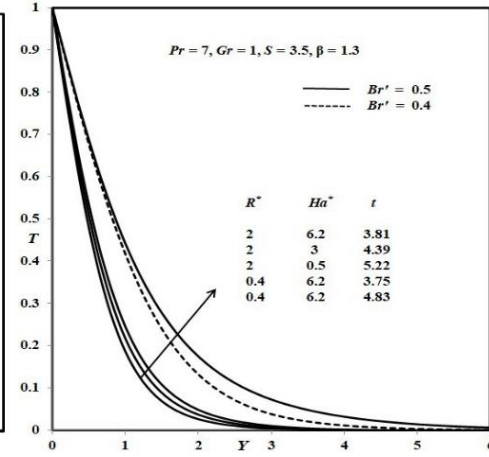


Fig. 4 – Temperature profile.

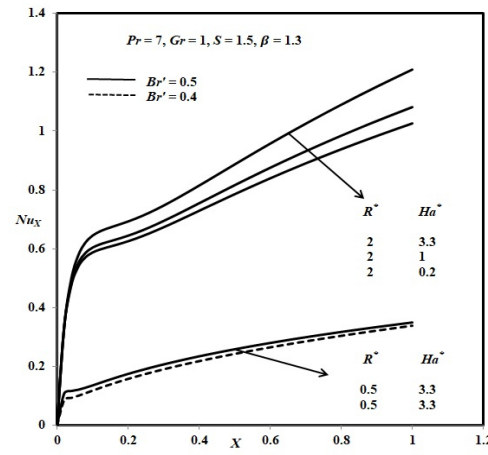
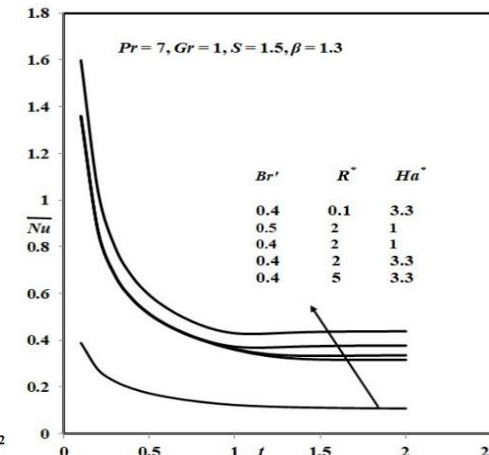


Fig. 5 – Nusselt number for various R^* , Ha^* and Br' in local and average sense.



In both local and average sense, Fig. 5 explains the Nusselt number values and Fig. 6 illustrates the viscous drag pertaining to the flow field. The Nusselt number values progressively improved as the flow is stimulated by the EMHD effects of Lorentz force while raising the modified Hartmann number Ha^* . However, this resistance force diminishes the skin friction between the surface and fluid molecule. The heat transfer rate is improved for the elevated values of Br' . Also, from elevated temperature to low temperature regions, radiation R^* improves the energy transfer between the molecules while it weakens the skin friction.

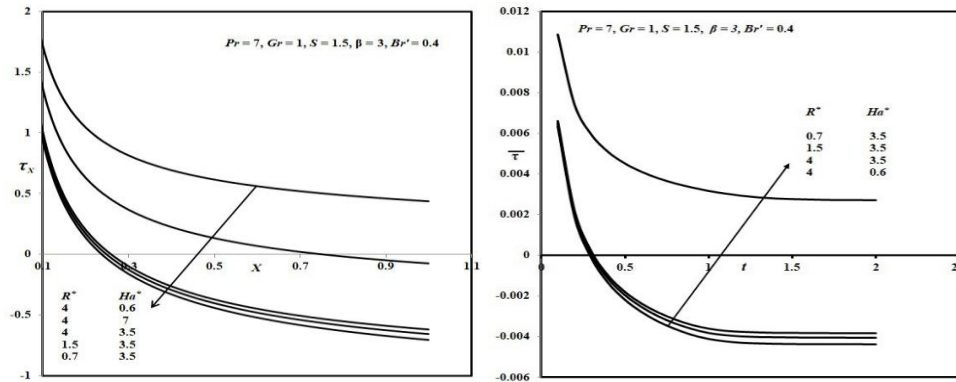


Fig. 6 – Skin Friction for various Ha^* and R^* in local and average sense.

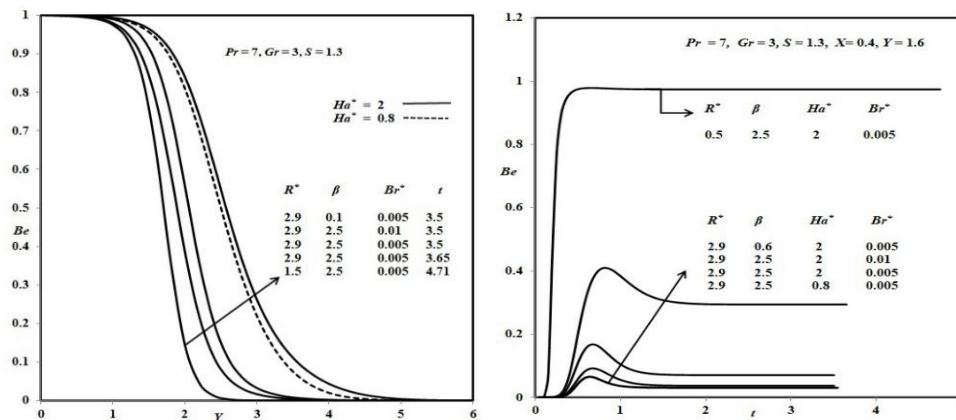


Fig. 7 – Variations of Bejan number and its transient profile.

Figure 7 shows the interdependence of entropy generation associated with fluid friction and heat transfer, as Bejan number defines the ratio of irreversibility contributed by the transfer of heat and the sum of irreversibility produced by heat transfer and friction between fluid layers. The Casson parameter with the higher intensity of yield stress slacken off the fluid friction. Consequently, the improved Casson parameter and modified Hartmann number uplift the Bejan number values. On the contrary, values of Bejan number diminish while elevating the values of radiation parameter and Br^* . Additionally, it can be noticed that the Bejan number values are bounded between 0 and 1. The entropy production on account of heat transfer has no significance when the fluid particles are far away from the surface. On the other hand, for the fluid particles in the vicinity of the plate, the entropy generation because of frictional effects between the layers of fluid is negligible. The iso-responses correspond to space variables are plotted in Fig. 7a. It is readily perceived that the projection of responses on 2D plane are broader when the values

of radiation parameter (R^*) and modified Brinkmann number (Br^*) deteriorate, while Casson parameter and modified Hartmann number shows the reverse outcome.

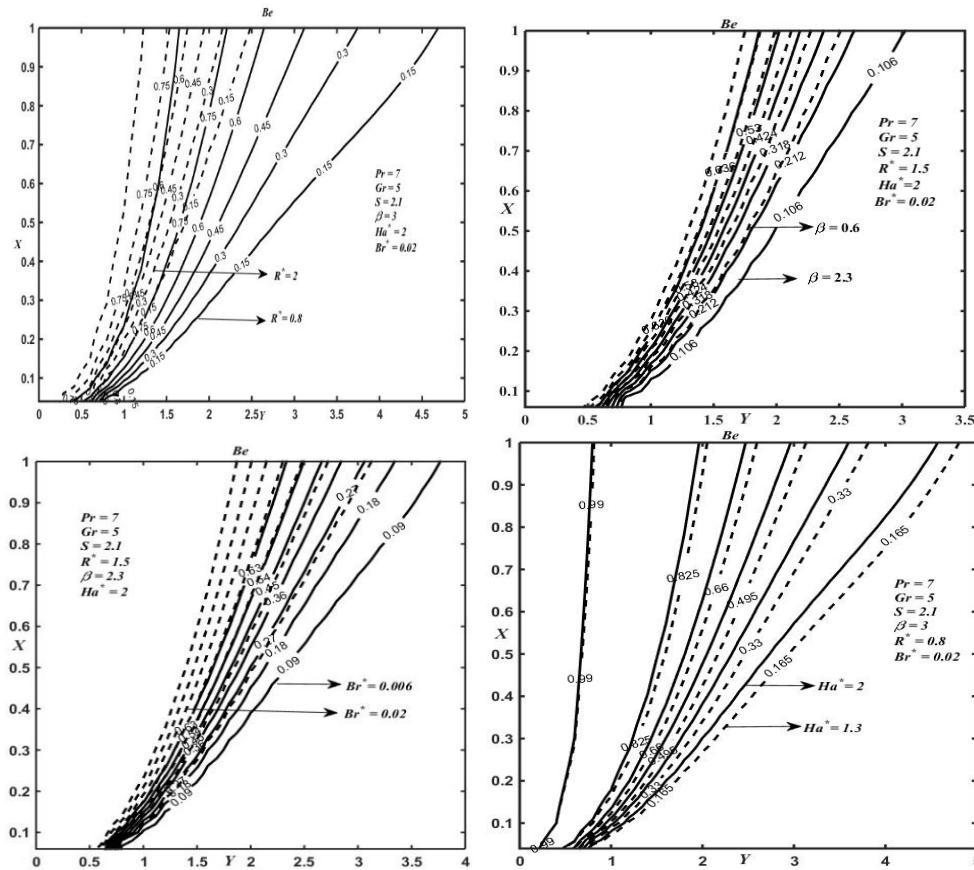


Fig. 7a – Contour Plots of Bejan number.

The entropy generation is illustrated in Figs. 8 and 8a. Viscous heat generation because of fluid friction and transmission of heat by virtue of radiative heat transfer exhibit a higher impact on production of entropy. The modified Brinkmann number describes the heat conduction with respect to the change in temperature. The heat transfer by conduction and radiation stimulates the entropy production. The plastic dynamic viscosity associated with the viscoplastic fluid slow down the entropy production. Also, the analysis of Nusselt number delineates the heat transfer ability is evolved for the improved modified Hartmann number. Thus, entropy generation is more rapid when there is a raise in modified Brinkmann number (Br^*) and radiation parameter (R^*). While on the contrary, the improved modified Hartmann number and Casson parameter weakens N_s^* .

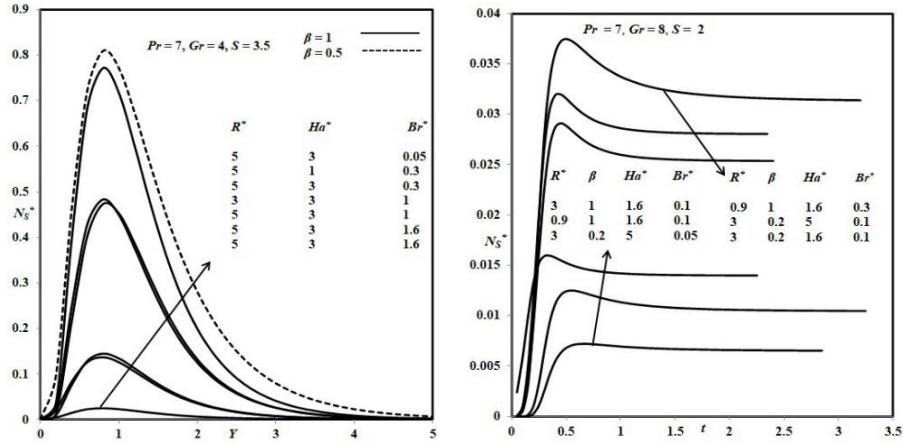


Fig. 8 – Entropy generation at steady state and transient state.

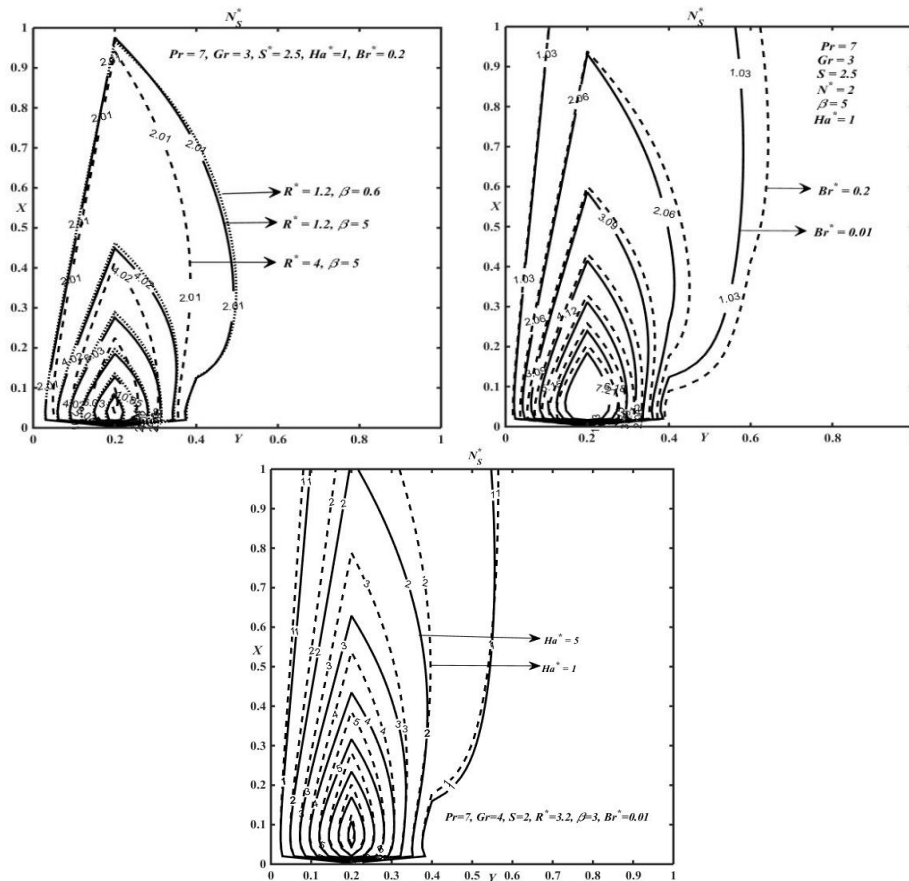


Fig. 8a – Contour plots of Entropy.

5. CONCLUSIONS

In studying entropy production of Casson fluid flow over a Riga plate, the following inferences are listed as concluding part of the analysis.

- The modified Hartmann number Ha^* that stimulates the aiding flow enhances the flow speed and assist the fluid flow to achieve the steady state faster. However, Ha^* diminishes the temperature distribution.
- The impact of EMHD instigates the heat transfer between fluid layers and dwindles the skin friction.
- The higher modified Hartmann number and Casson parameter aim to curb the generation of entropy. On the other hand, modified Brinkmann number and radiation parameter shoots up the entropy.
- As the Bejan number quantifies the potential of entropy generation because of heat transfer and fluid friction, the modified Hartmann number and Casson parameter elevate the Bejan number while it is decaying with respect to Br^* and R^* .

NOMENCLATURE

a^* – Absorption coefficient [m^{-1}]	t' – Time [s]
Be – Bejan number	T' – Temperature [K]
Br' – Brinkmann number	T – Non dimensional temperature
Br^* – Modified Brinkmann number	v – Velocity in transverse direction [ms^{-1}]
Gr – Grashof number	u – Velocity in vertical direction [ms^{-1}]
Ha^* – Modified Hartmann number	U – Non dimensional vertical velocity
g – Gravitational acceleration [ms^{-2}]	V – Non dimensional horizontal velocity
J_0 – Current density [Am^{-2}]	x – Vertical space coordinate [m]
l – Width of the magnets and electrodes, [m]	X – Non dimensional vertical spatial coordinate
M_0 – Magnetization of the magnets, [$kg A^{-1}s^{-2}$]	y – Transverse coordinate [m]
N_s^* – Non dimensional entropy generation	Y – Non dimensional transverse coordinate
Nu_x – Local Nusselt number	<i>Greek symbols</i>
\overline{Nu} – Mean Nusselt number	α – Thermal diffusivity [m^2s^{-1}]
Pr – Prandtl number	β – Casson parameter
R^* – Radiation parameter	β' – Coefficient of thermal expansion [K^{-1}]
S_G – Characteristic entropy generation rate	σ' – Stefan-Boltzmann constant [$Wm^{-2}K^{-4}$]
T'_w – Temperature at the wall	κ – Thermal conductivity [$Wm^{-1}K^{-1}$]
T'_∞ – Temperature at ambient condition	τ_x – Skin friction coefficient in local sense
t – Dimensionless time	$\bar{\tau}$ – Mean skin friction coefficient

REFERENCES

1. A. Selamat and V. S. Arpaci, *J. Thermophys. Heat. Transfer* **4**, 404–407 (1990).
2. A. Bejan, *J. Appl. Phys* **79**, 1191–1218 (1996).
3. A. Butt, S. Munawar, A. Ali, and A. Mehmood, *J. Mech. Sci. Technol* **26**, 2977–2984 (2012).
4. R. Ellahi, S. Z. Alamri, A. Basita, and A. Majeeda, *J. Taibah Univ. Sci.* **12**, 4, 476–482 (2018).
5. S. E. Ahmed, M. A. Mansour, A. Mandy, and S. S. Mohamed, *Eng. Sci. Technol. Int. J.* **20**, 1553–1562 (2017).
6. L. B. Erbay, M. S. Ercan, B. Sulus, and M. Murat Yalçın, *Entropy* **5**, 506–518 (2003).
7. L. B. Erbay, M. M. Yalcin, and M. S. Ercan, *Heat Mass Transfer* **43**, 729–739 (2007).
8. A. Réveillère and A.C. Baytaş, *Int. J. Exergy*, **7** 164–177 (2010).
9. J. A. Esfahani and M. M. Jafarian, *Sci. Iran*, **12** 233–240 (2005).
10. M. H. Matin, *J. Mech. Eng. Autom.* **5** 26–32 (2015).
11. M. Ferhi and R. Djebali, *Rom. J. Phys.* **67** 605 (2022).
12. F. Irgens, *Rheology and Non-Newtonian fluids*, Springer, New York, 1995.
13. G. W. Scott Blair, *Rheol. Acta* **5**, 184–187 (1966).
14. P. Chaturani and R. P. Samy, *Biorheology* **23**, 499–511 (1986).
15. V. P. Srivastava and M. Saxena, *J. Biomech* **27**, 921–928 (1994).
16. R. K. Dash, K. N. Mehta, and G. Jayaraman, *Int. J. Eng. Sci.* **34**, 1145–1156 (1996).
17. G. Gopi Krishna, S. Sreenadh, and A. N. S. Srinivas, *World Appl. Sci. J.* **35**, 1059–1067 (2017).
18. M. A. Mansour, A. E. Sobhy, M. Mahdy, S. E. Ahmed, and S. S. Mohamed, *Walailak J. Sci. Tech.* **14**, 169–187 (2017).
19. O. Posdziech and R. Grundmann, *Eur. J. Mech. B/Fluids* **20**, 255–274 (2001).
20. E. Magyari and A. Pantokratoras, *Commun. Nonlinear. Sci. Numerical Sci.* **16**, 3158–3167 (2011).
21. A. Pantokratoras, *Math. Probl. Eng.* **2008** (2008).
22. P. Loganathan and K. Deepa, *J. Theor. Appl. Mech.* **57**, 987–998 (2019).
23. P. Loganathan and K. Deepa, *Nonlinear Anal. Model. Control* **25**, 443–460 (2020).
24. K. Rafique, H. Alotaibi, N. Ibrar, and I. Khan, *Energies* **15**, 316 (2022).
25. M. Rooman, M. A. Jan, Z. Shah, P. Kumam, and A. Alshehri, *Sci. Rep.* **11** (2021).
26. Z. Shah, M. R. Hajizadeh, Ikramullah, N. A. Alreshidi, W. Deebani, and M. Shutaywi **117** (2020).
27. H. Wang, F. Liu, H. Zhai, and K. Wang, *Act. Mater.* **60**, 1444–1454 (2012).
28. L. M. Martyushev and V. D. Seleznev, *Cur. Opin. Chem. Eng.* **7**, 23–31 (2015).
29. E. M. Arthur, I. Y. Seini, and L. B. Bortteir, *J. Appl. Math. Phys.* **3**, 713–723 (2015).
30. K.U. Rehman, A. A. Malik, M. Y. Malik, N. Sandeep, and N. U. Saba, *Results Phys.* **7**, 2997–3006 (2017).
31. M. Q. Brewster, *Thermal radiative transfer and properties*, John Wiley and Sons, New York, 1992.
32. W. G. England and A. F. Emery, *J. Heat Transfer* **91**, 37–44 (1969).
33. B. Carnahan, H. A. Luther, and J.O. Wilkes, *Applied Numerical methods*, John Wiley and Sons, New York, 1969.
34. A. Pantokratoras and E. Magyari, *J. Eng. Math.* **64**, 303–315 (2009).
35. B. Gebhart and L. Pera, *Int. J. Heat Mass Transfer* **14**, 2025–2050 (1971).